Computer simulations of laser ablation sample introduction for plasma-source elemental microanalysis

Davide Bleiner* and Annemie Bogaerts

Received 31st May 2006, Accepted 29th August 2006
First published as an Advance Article on the web 14th September 2006
DOI: 10.1039/b607627k

Elemental microanalysis, using laser ablation for sample introduction into plasma-source spectrometry, is based on the analytical information carried by the ablated particles that are delivered to the ICP. Numerical fluid-dynamical simulations allowed us to understand the flow characteristics of the carrier gas, which influence the sample introduction and signal intensity. The carrier gas flow in the transport tubing was found to be laminar, with nested velocity paraboloids, whose front profile is less sharp for heavier carrier gases. The gas velocity is also characterized by high-frequency fluctuations along the tube length due to molecular diffusion. The temporal signal profiles were modelled considering the aerosol filling and elution rates in the setup, the whole setup dimensions, the transport efficiency, and the particle sizes, combined with a condition of mass conservation. The simulated signal intensity showed a logarithmic dependence on the transport efficiency, which exacerbates signal structure. Finally, in passing from single shot to repeated shot analysis, the transient signals were modelled calculating the convolution of the single shot profile with the laser pulse sequence profile.

Introduction

Laser ablation is a powerful technique for solid sample introduction into inductively coupled plasma (ICP) optical emission spectrometry (OES) or mass spectrometry (MS), facilitating spatially resolved elemental and trace analysis of any kind of sample.[1–3] The working principle is straightforward, *i.e.*, a sample is laser-irradiated in a flowing ambient gas, which is Ar or He, so that the laser ablated aerosol is transported to the ICP discharge for atomization and excitation/ionization. In the following we will refer to ICP-MS analysis, but analogous considerations apply to ICP-OES, since the scope of this paper is focused on the sample introduction stage.

The LA-ICP-MS signal profile results from the combination of *operating conditions* and *ablation setup* characteristics. The signal profile influences the analysis because it determines the signal-to-noise ratio (SNR), the detection limit (DL), and the depth resolution in depth profiling analysis. Hence, a theoretical understanding of the signal structure dependence on the various operating parameters is also important for practical reasons. First, it will permit the development of efficient strategies for data processing, *e.g.*, signal deconvolution, extraction of true depth profiles, particle-related effects, correction for fractionation or matrix-bias. Second, it might help to identify potential sources of error, which are not directly related to the laser–sample interaction or particle vaporization in the ICP discharge, or even ion detection.

The aim of this work was to investigate LA sample introduction using computer simulations, so that specific parameters could be studied independently, especially when the space or time scale is experimentally challenging. The results were oriented toward two aspects, namely the investigation of the carrier gas flow characteristics (*e.g.*, velocity, pressure) and the relation of parameter settings to the signal intensity profile. These results will be critically related to previously reported experimental results, showing that the present model improves our understanding of the process. For the first time, the *particle size* will be considered as a variable and its effects on transport efficiency and signal characteristics will be shown. Moreover, the *transport efficiency* will also be included in the equation for signal intensity profile, showing that its importance has been so far underestimated. First, an overview of literature results related to the issue of the LA-ICPMS signal profile is given.

University of Antwerp, Department of Chemistry, Universiteitsplein 1, BE-2610 Antwerp, Belgium. E-mail: davide.bleiner@ua.ac.be

Background

In the late 1980s, Moenke-Blankenburg and her group[4–7] presented the first systematic investigations on the effect of the laser ablation setup on the ICP-OES signal profile. The work was based on experimental results, which were subsequently interpreted theoretically. Thereafter, the authors suggested possible changes to apply at the setup, in order to improve the analytical performance. The signal characteristics, determined for single shot delivery in combination with ICP-OES, were shown to be highly influenced by the geometry of the setup. One notable change to it was the implementation of the single bead string reactor (SBSR), in order to homogenize the velocity profile across the tube cross section, and minimize signal dispersion. The SBSR was obtained filling a transport tubing with spheres of up to 80% of the tube diameter. The friction operated on the forward motion of the carrier gas was presumed to avoid the formation of a pronounced parabolic velocity profile. The use of a SBSR was

reported to lead to sharper signals as compared with the free tube transport condition.[4]

In the early 2000s, Bleiner and Günther[8,9] investigated experimentally the effect of setup geometry on single shot signal characteristics in combination with ICP-MS, and combined these observations with a theoretical description. A significantly different signal structure was shown as a function of set-up volume, most notably influenced by the cell volume and shape. However, the signal area was approximately unchanged for cells up to 100 cm^3, indicating that mass transport efficiency could be maintained, though under different transport speeds and flush rates.

The theoretical relation was developed by considering the product of the *cell-related* elution function and the *tube-filling* function, which resulted in a pulse-shaped function. An acceptable matching between experimental results and theoretical prediction was attained, especially for the large volume cells. The two functions were adopted from refs. 4–7 and are *independent* function typologies, *i.e.*, the cell-related one is an exponential decay function of the kind $e^{-f(t)}$ and the tube-related one is a fractional linear function of the kind $[1-f(1/t)]$. However, a careful analysis reveals that the two functions cannot be fully heterogeneous, due to mass conservation in the transport set-up. In fact, since the mass that exits the cell must be found in the tube, a mass balance between the two functions must hold at any time. Thus, the tube-related function must be complementary to the cell-related function.

Plotnikov *et al.*[10] have used an analytical equation that fulfils this requirement, to perform improved data fitting. Unfortunately, the function was presented without physical derivation, as is found in commercially available data reduction software packages (*i.e.*, *Microcal Origin*®). Extensive discussion on this equation is presented below.

Leach and Hieftje[11] explored experimentally the effects on transient pulse width of ablation-cell volume, the diameter and length of tubing used to connect the ablation cell to the detection unit, and the type and flow rate of the carrier gas. Minimization of ablation-cell volume and the length and diameter of the transfer tube was reported to dramatically decrease the peak widths of transient signals. Besides, the use of He to transport analyte particles from the ablation cell reduced the effect of cell volume on signal width. The use of a cell volume of 0.70 cm^3 and optimization of all instrumental parameters produced a transient signal of 0.085 s in duration and limits of detection in the tens of fg range, for single-shot laser-ablation.

Recently, Gäckle and Mertens[12,13] proposed a transport model for the LA-ICP-MS temporal intensity distribution derived from the original contributions in refs. 4–7, both in single-shot and multiple pulses. The assumption was that a laminar flow would allow the flow of aerosol along concentric streamlines in the tubing. The assumption was motivated by the condition that the gas speed must be less than 20% of the speed of sound,[12,13] which actually only permits the conclusion that the flow is incompressible, not that the flow is necessary laminar. In fact, the *Reynolds number (Re)*, commonly used as a selection criterion for laminar ($Re < 2100$) or turbulent flow ($Re > 2100$), is a function of fluid speed v and also tube diameter D, fluid's density ρ and dynamic viscosity μ (*i.e.*, $Re = vD\rho/\mu$). Hence, one can easily calculate that the condition $Re = 2100$ in a common 4 mm id tubing would be already attained at an Ar carrier-gas velocity of 5.2 m s^{-1}, *i.e.*, the threshold velocity for turbulence onset is as low as 2% of the speed of sound.

The signal dispersion function, *i.e.*, the ratio between the pulse intensity and an equivalent rectangular pulse intensity,[14] has been found to be linearly related to the transport time in the centre of the transport tube, to the carrier gas flow rate, the chamber volume, and the ratio between carrier gas flow rate and ablation chamber volume.[12,13] Unfortunately, the given equation did not satisfy continuity, for similar considerations made above for refs. 8 and 9. The authors explained the mismatch between theory and experiment with the hypothesis that only the central part of the transported aerosol was observed at the detector,[12,13] which suggests aerosol loss along the setup walls or incomplete ICP atomization.

So far, a common feature of all published models is that the particles that are produced during laser ablation have been assumed to be point-like, *i.e.*, the size distribution has been neglected, thus developing a description for a homogeneous fluid phase. However, it is well known that the particle size distribution of the aerosol (*i.e.*, the discrete phase) spans over three orders of magnitude, namely in the range 10 nm–10 μm.[15] Thus, the influence of the discrete phase also needs to be included, for a complete description of the LA-ICP-MS signal profiles.

The computational models

The simulations were realized using two different codes, a numerical one for computational fluid dynamics (CFD) and an in-house-written analytical one for the intensity signal profiles. The former is solved by points from a collection of conservation equations (Navier–Stokes). The latter implements an exact solution which is by nature a curve function.

The CFD calculations were performed with FLUENT 6.2, which is a commercially available software package that allows one to compute gas flow characteristics in a certain computational domain. The computational domain was created with the GAMBIT 2.2 software for the development of computational meshes. Calculations with FLUENT 6.2 permitted us to obtain insights on the gas flow, velocity, pressure, *etc.*, in the transport tubing. The calculations were performed to shed light on the carrier gas as the important aspect of sample introduction.

A parallel computational session was a self-written original code that was used to model the profile of the intensity signals, as well as to obtain better insights into the effect of operating parameters on transient signal characteristics. The plots used to model signal profile as a function of time are presented as counts per second (cps), *i.e.*, as obtained from the number of particles delivered to the detection unit. On the other hand, the signal intensity as a function of parameter's setting (*e.g.*, flow rate, tube size, *etc.*) is shown in time-integrated counts, for an integration time of 2 s. Since this was a deterministic code, solving analytically a set of differential equations, signal noise is not included, and the background value is zero, with smooth signal profiles.

One has to clearly understand the perspective of the two codes, *i.e.*, from what information one is starting and what one wants to obtain. The CFD code was used to investigate the carrier gas flow and particle transport. The in-house-written code was devised to obtain spectrometric insights, *i.e.*, results on transient signal profiles. There is no conflict between the two, because they are designed to perform different tasks. In the following, we want to describe the mathematical relations that have been included in the CFD code, as well as those which have been newly developed and introduced for the in-house-written signal profile code. We will also provide some comparison on literature results, to show the requirement for a novel mathematical treatment of the signal profile.

The code for CFD calculations

In LA-ICP-spectrometry the laser-induced aerosol is transported by a moving fluid phase that fills the setup volume, and is set into motion by a pressure gradient. The first issue to address is the description of the motion of the carrier gas. Subsequently, one can add in the treatment an ensemble of particles that move along the stream.

The Navier–Stokes equation governs the motion of the fluid phase, in the sense of balance of momentum changes as a function of pressure and dissipative viscous forces inside the fluid. For constant viscosity (η) and mass density of the fluid (ρ_f), where the condition of incompressibility is valid for flow speed less than 0.3 Mach (*i.e.*, approximately 100 m s^{-1}), one obtains the following momentum equation:

$$\rho_f \frac{\mathrm{d}\vec{v}}{\mathrm{d}t} = -\nabla \cdot \vec{p} + \eta \cdot \nabla^2 \vec{v} + \rho_f \vec{g} \qquad (1)$$

where ρ_f is the gas mass density, v is the gas velocity, t is time, p is pressure, η is viscosity and $g = 9.81$ m s^{-2}.

The gas velocity profile was shown previously[8] to be parabolic, and given by the following velocity distribution equation:

$$v(r) = \frac{2F}{\pi R^2}\left[1 - \left(\frac{r}{R}\right)^2\right] \qquad (2)$$

where F is the gas flow rate, R is the tube radius, and r is the radial distance from the tube axis. Eqn (2) shows that the maximum velocity is along the tube axis at $r/R = 0$, with the mean velocity that is the half of the maximum velocity. This ideal laminar parabolic profile is valid as long as a fully developed flow is obtained. In the case of turbulent flows the velocity profile would be more homogeneous at the centre, with a thin boundary layer.[16] The parabolic profile develops dynamically from the initial flat profile at the tube entrance (so-called *free stream flow*) over an entry distance. Across this entry distance, there is a shear stress region close to the tube walls, *i.e.*, a region of rapid velocity change, which is called *boundary layer*. The thickness of the boundary layer is widely accepted[16,17] as the radial distance from the tube wall (where the gas velocity is zero) to the point where the velocity is 99% of the free stream velocity. The value of the boundary layer thickness increases from the tube entrance downstream until the flow becomes *fully developed*. This dynamic evolution influences the gas velocity profile as well as the transport of the LA-induced particles (sample introduction).

The treatment of solid particles that move along the fluid phase is complex. Due to the physical heterogeneity of the particle ensemble, the various forces acting on the particles might be less or more significant depending on their size and shape.[18] Here, it is convenient to organize the discussion in a schematic way, first addressing the types of forces, and then combine this information discussing particle dynamics.

Fluid–particle forces. The most important of the hydrodynamic forces is the *drag force*, *i.e.*, the resistance for the particle to move at a different speed, faster or slower, through the embedding fluid. This force results from a so-called *form component*, due to the cross-section exposed normal to the fluid flow, and a so-called *frictional component*, due to the velocity difference between the fluid and the particle. The mathematical expression of the drag force is different depending on the flow regime, *i.e.*, whether turbulent (*i.e.*, the Newton's drag region), or laminar (*i.e.*, the Stokes' drag region). As shown below, the flow regime is, in our case of LA-ICP-spectrometry, close to the Stokes' region and we focus here on its analytical expressions (although the FLUENT program can deal also with turbulent flows). For aerosol transport realized in the Stokes' regime, the expression for the drag force is as follows[18]

$$\vec{F}_{\mathrm{drag}} = -\frac{3\pi\eta d_p(\vec{v}_p - \vec{v}_f)}{C_{\mathrm{slip}}} \qquad (3)$$

where d_p is the particle diameter, and the subscripts to velocity refer to the particle (p) and the gas (f). A parametric relation gives the slip correction factor (the so-called Cunningham factor) as follows:

$$C_{\mathrm{slip}} = 1 + Kn(A_1 + A_2 e^{-A_3/Kn}) \qquad (4)$$

where Kn is the Knudsen number, *i.e.*, the ratio between the mean free path of the continuous phase and the particle radius.[19] The slip correction coefficient C_{slip} is particularly important for sub-micron particles, because the particle radius becomes comparable with the fluid mean free path, and the assumption of zero gas velocity at the particle surface (valid for larger particles) is no longer valid (*slipping effect*). The coefficients A_1, A_2, A_3 in eqn (4) are experimental values that suit to the specific physical system. Buckley *et al.*[20] have provided the following set of values for all solid particles sizes, accurate within 2%: $A_1 = 1.099$, $A_2 = 0.518$, $A_3 = 0.425$. The obtained expression for the slip coefficient is in agreement with the one suggested previously in Allen and Raabe,[21,22] where another set of values was used.

A further hydrodynamic force included in the CFD code is the so-called *virtual mass*,[17] which is the additional inertia of the actual particle mass, due to the surrounding sticking fluid. However, such a force becomes significant only when the dispersed phase density is smaller than the fluid phase density. Hence, this virtual mass is less significant in our simulations. The *Basset force*[17] is another hydrodynamic force, which is associated with past acceleration processes on the particle. Similar to the virtual mass, this force can also be considered less important for high particle-to-fluid mass density ratios. Further hydrodynamic forces induce a lift in the particle, *i.e.*, an acceleration along a direction perpendicular to the motion

direction. The *Magnus force* is associated with the rotation of the particle and the consequent inhomogeneous pressure distribution over the surface. The differential pressure across the particle surface induces a lift which, combined with the forward motion, produces a curved trajectory (*i.e.*, 'the soccer ball' effect). Rubinov and Keller[23] provided an analytical expression for the Magnus force, where one notes that the proportionality on relative forward and angular velocity (relative between the particle and the fluid), as well as the dependence on the particle surface, make this force less significant for small round particles. Lift can also be caused by shear in the fluid flow. Saffmann first[24] and later Li and Ahmadi[25] investigated the mechanism, and a mathematical relation for a transverse lift force (so-called *Saffman force*) was given, which has been implemented in the CFD code.

Finally, the forward motion of the particle along the transport tubing is supported by the pressure gradient. For small particle sizes, and for laminar flows, we can assume a constant pressure gradient in the surroundings of the particle and thus integrate the pressure forces over the particle surface and obtain:

$$\vec{F}_{\text{press}} = -m_p \frac{\nabla \vec{p}}{\rho_p} \tag{5}$$

where m_p is the particle mass and ρ_p is the particle mass density.

Particle–particle forces. A second class of forces arises through particle interactions, *e.g.*, forces due to collisions, either with other particles or with the walls, and Coulomb forces. The particle-to-particle collision frequency is the product of particle velocity, particle size (collision cross section) and particle number density. Inter-particle collisions commonly lead to a rapid variation of the velocity vector. In some more peculiar cases they can induce coagulation, especially in combination with other forces that favour inter-particle binding. The presence of a surface charge, as potentially induced during the ablation, supports or contrasts such processes, depending on polarity. However, to-date there are no experimental investigations on electrostatic characteristics of LA aerosols at atmospheric pressure for ICP-MS analysis and thus any discussion on this aspect seems to be premature. Hence, particle agglomeration has not been considered in our simulations.

In conclusion, the particle forces discussed so far need to be summed vectorially, also considering the *gravitational force*. To make the notation more compact, we group several recurring constants in the following expression, which is useful to simplify the expression of the drag force:

$$\phi = \frac{3\pi\eta d_p}{C_{\text{slip}} m_p} \tag{6}$$

which has the dimensions of a flow rate per unit mass density (*i.e.*, s^{-1}). Finally, we obtain the particle dynamics balance among pressure drop (first term of right-hand side), drag viscous force (second term), gravitational force (third term) and lift forces (fourth term) with the following first order partial differential equation on space and time variables:

$$\rho \frac{\mathrm{d}\vec{v}_p}{\mathrm{d}t} = -\nabla \cdot \vec{p} - \rho_p \phi \cdot (\vec{v}_p - \vec{v}_f) - (\rho_p - \rho_f)\vec{g} + \vec{F}_{\text{lift}} \tag{7}$$

The solid particle density is much higher than the gas density, so that the density difference can be reasonably approximated to $\rho_p - \rho_f \approx \rho_p$. The lift force can be neglected, if the shear flow is constant all over the particle surface, and the particles are too small for any significant Magnus force to apply.

The original code for the transient signal profile

Under ideal conditions, the ablation, transport, and ICP atomization of the sample are instantaneous processes (*delta function*), so that no signal dispersion is introduced. In real experiments, we have to deal with a combination of signal dispersion factors that contribute to the final observed profile width. Considering the whole sample introduction process, such factors can be generally attributed to the duration of the *laser pulse*, the duration of the setup *elution* period, and the duration of the ICP *atomization*.

The duration of the laser pulse is 8 or 9 orders of magnitude shorter than the whole sample introduction process, *i.e.*, 6–20 ns pulse width *versus* 1–2 s for the sample introduction or single shot signal dispersion. Thus, the laser pulse can be assumed to be instantaneous, which will not affect the elution signal profile.

The duration of the ICP-atomization is a fraction of the particle residence time, depending on the volatility of the analyte. The particle residence time is of the order of a few tens of ms,[26] thus it can be assumed to be the *pristine time-spread* of signal generation in the whole LA-ICP-MS system. However, as far as the ICP spatial distribution of atom population is concerned, there is a further influence on the observed signal profile. In fact, depending on the ICP sampling depth, signal characteristics might vary in response to different local ICP stoichiometries. However, this topic deserves specific studies and is considered to be outside of the scope of the present article, where we treat the ICP-MS with normalized sensitivity.

Finally, the entrainment and transport of particles out of the sample chamber, and their introduction into the ICP torch, is the temporally relevant process. This process is far from being a "delta function", due to diffusion processes that take place in the whole ablation setup. Hence, the ability to understand the intensity *versus* time dependence of transient signals offers great control over the whole experimental capability.

The use of pulsed lasers has introduced great flexibility into the sampling procedure. In fact, one can choose the number and the rate of delivery of pulses, in order to control the amount of mass to analyze or the sampling depth. Depending whether one single laser shot or multiple pulses are delivered, the signal structure will vary significantly. Therefore, the two situations will be discussed in separate sections.

Single shot. The temporal intensity profile obtained in single shot LA-ICP-MS is a time-of-flight-type (TOF) profile of the aerosol delivery. The number of transported particles per unit time contributes to obtaining the experimental signals. The fact that such a response is also a function of specific analytical

and ICP conditions has been investigated elsewhere.[27] In the following treatment, we normalize our signals and consider the instrumental response equal to one. Important aspects to an accurate description of the signal profile are (*i*) the complete description of the *flush rate* of the set-up and (*ii*) the fact that the analytical expression complies with *mass conservation*. These two issues were investigated carefully and a novel analytical expression could be obtained. Therefore, before providing a mathematical expression for the transient signal profile as a function of time, we need to discuss these two aspects.

The setup *flush rate* was previously defined as a ratio between the gas flow rate and the ablation cell volume, *i.e.*, $k = F/V_{\text{cell}}$.[4–8] In this work we want to obtain a complete expression for the flush rate that also includes the aerodynamics of the entire setup. As starting point for this discussion, we observe that the change of particle number in the setup is a function of (time-dependent) particle number density. That is to say that when many particles are in the setup, these elute fast, which steadily decreases the particle number density in the setup, and so the elution speed. This is described by a first order rate equation, with general solution $N_t = N_0\ e^{-k\Delta t}$. From this solution, which is the exponential elution law, one can solve on the rate constant k and obtain the so-called flush rate:

$$k_{\text{flush}} = -\frac{1}{\Delta t}\text{Ln}[N_t/N_0] \qquad (8)$$

The temporal interval Δt of eqn (8), *i.e.*, the time passed between the start of the flush process and the observation instant, can be obtained as a ratio between the effective volume that is flushed (*i.e.*, V_{eff} in m^3) and the flow rate (*i.e.*, F in $\text{m}^3\ \text{s}^{-1}$). The *effective volume* is the total volume of the ablation setup minus the dead volume. The total volume refers to the geometric volume of the setup, *i.e.*, the sum of cell volume (V_{cell}) plus tube volume (V_{tube}). For the most common setups, $V_{\text{geom}} = V_{\text{cell}} + V_{\text{tube}} \approx V_{\text{cell}}$, since the volume of the tube is much smaller than that of the cell. The *dead volume* is the sum of the space occupied by the target sample(s), plus the regions that are not swept by the carrier gas, due to the specific fluid-dynamics pattern. In conclusion, the pre-logarithmic factor of eqn (8) can be expressed as a function of experimental parameters as follows: $1/\Delta t = F/V_{\text{eff}}$.

The N_t/N_0 argument of eqn (8) is the ratio between the not-yet eluted mass that is still inside the setup at the end of the time Δt, and the total ablated mass N_0. To simplify, we can introduce the aerosol transport efficiency as the ratio of eluted mass over the total mass, *i.e.*, $\varepsilon = (N_0 - N_t)/N_0$. Hence, the logarithmic argument of eqn (8) can be written as $(1 - \varepsilon)$. Therefore, we obtain from eqn (8) an accurate and experimentally complete definition of the flush rate implementing the considerations made here, such as the following:

$$k_{\text{flush}} = -\frac{F}{V_{\text{eff}}}\text{Ln}(1 - \varepsilon) \qquad (9)$$

where the minus sign should be combined with the calculation of the log factor, since the mere log factor $\text{Ln}(1 - x) < 0$ for $0 < x < 1$.

Note that the present definition of the flush rate is accurate, and matches the one from refs. 4–7 in the special case of small samples, in efficiently swept setups (*i.e.*, $V_{\text{dead}} \sim 0$), with a transport efficiency of approximately 63%, where the log-factor is equal to one. The present formula with the logarithm of the transport efficiency indicates that at identical setup volume, a setup with improved transport efficiency provides sharper signal profiles, due to optimized flow dynamics. Thus, the original definition from refs. 4–7 underestimated the importance of the flow pattern across the setup, in favour of mere geometric considerations, a limitation that the present description helps to overcome.

Mass conservation needs to be discussed now. In ref. 10, the signal intensity profile was successfully fitted to experimental data using a pulse function defined as the product of two exponential functions, as follows:

$$I_{\text{pulse}}(t) = I_0 e^{-\frac{t-T_0}{\tau_1}}(1 - e^{-\frac{t-T_0}{\tau_2}})^p h(t - T_0) \qquad (10)$$

This expression is a generalization of the specific analytical description of transient signal intensity profiles, and we want to provide a physical meaningful discussion for that. Eqn (10) includes two flush rates, one for the signal decay (*i.e.*, $k_1 = 1/\tau_1$, with τ being the time constant) and one for the signal rise (*i.e.*, $k_2 = 1/\tau_2$), which implies that the evacuation and filling are realized at two different speeds. However, for mass continuity, the two time constants τ_1 and τ_2 must be identical in LA-ICP-MS setups. If the values of τ_1 and τ_2 are different, we have to conclude that the ablation setup is not tight or leak-proof, and mass might be either lost ($\tau_1 < \tau_2$) to or added ($\tau_1 > \tau_2$) from the exterior.

The exponent p in eqn (10) derives from a rather complicated generalization, and must here be considered equal to one, for typical LA-ICP-MS setups. It stands for the number of *input reservoirs*, *e.g.*, number of sampling sites ablated at the same time. In fact, if the $e^{-f(t)}$ term stands for the exponential loss of signal intensity with time, the $(1 - e^{-f(t)})$ term stands for the aerosol feeding, *i.e.*, increase of signal intensity with time. In the case of multiple ablation spots merging their aerosol batches into the same tubing at the same time, the $(1 - e^{-f(t)})$ term must be computed more times and raised to the power $p > 1$.

Such a description, with the specific comments made here, gives results that are mathematically and physically appropriate, more so than those published earlier.[8] Although in ref. 8 the experimental fits seemed to suggest a good match between theory and experiment, it was an approximated result for large volume setups, as can be demonstrated. A comparison of the two functions, *i.e.*, the one with the *linear fractional term* $(1 - T_0/t)$ of refs. 8 and 9 and the one with the *co-exponential* $(1 - e^{-f(t)})$ term from ref. 10 and this present work, shows that the two have common points only in the special case where the ablation setup volume is large, *i.e.*, the flush rate k_{flush} is small. Fig. 1 shows single shot signal profiles generated with the linear fractional function (reported in ref. 8) and the one using the exponential term developed in this work (eqn (11), fully explained below). In the top panel we show the signals for the case of large volume ablation setup with flush rate $k = 0.5$, whereas in the bottom panel signals for

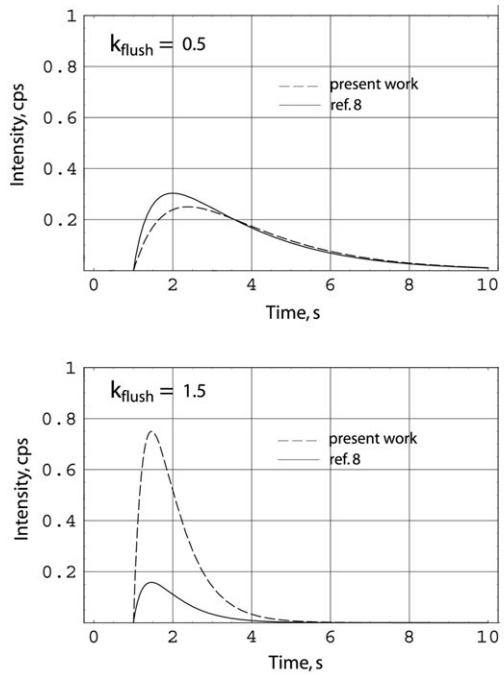

Fig. 1 Comparison of LA-ICP-MS signal profiles generated using the model of ref. 8 and the in-house written code of this work. In the top panel, signals associated with large ablation cells (flush rate $k = 0.5$) are simulated showing a small mismatch between the two models. In the bottom panel, signals associated with the use of small cells ($k = 1.5$) are simulated, showing a more significant mismatch between the two models. Note also that the dashed curve (present work) keeps the integral constant in both cases (mass conservation), whereas the description from ref. 8 does not.

the two models in a small ablation setup with $k = 1.5$ are shown. It is evident that the mismatch in the predicted signal profiles is modest in the former case. This means that the equation presented in ref. 8 is an acceptable approximation of the true function for large ablation cells or large transport tubing. In the case of ablation setups of small signal dispersion, or even in the case of in-torch ablation,[29,30] the mismatch between measured and predicted signal profile becomes more significant if the model of ref. 8 is used. The accuracy of the eqn (10) model in fitting experimental results has been already shown in detail in ref. 10.

It should also be noted that a change of the flush rate constant, as shown in the two panels of Fig. 1, re-shapes the profile but the total area under the curves (signal integral) should remain constant (*i.e.*, mass conservation requirement). It is clear from Fig. 1 that this is not the case for the model of ref. 8, demonstrating again that the mass was not mathematically conserved. The curves obtained with the present model, however, correctly obey mass conservation, as the areas under the curves are identical.

Thereafter, a complete LA-ICP-MS signal profile function can be derived from eqn (10) as a product of different distribution functions, as follows:

$$I(t) = \Re_{\mathrm{ICPMS}} \cdot 2k_{\mathrm{flush}} \cdot e^{-k_{\mathrm{flush}}(t-\mathrm{tof})}[1 - e^{-k_{\mathrm{flush}}(t-\mathrm{tof})}] \cdot h(t - \mathrm{tof}) \quad (11)$$

Eqn (11) includes the ICP-MS analyte-specific response factor (here $R_{\mathrm{ICPMS}} = 1$), the aerosol elution profile according to the exponential filling ($1-e^{-k_{\mathrm{flush}}(t-\mathrm{tof})}$) and evacuation ($e^{-k_{\mathrm{flush}}(t-\mathrm{tof})}$) of the setup, and the particle time-of-flight derived from their velocity. In fact, the particle time-of-flight (TOF) is the particle-dependent transport time in the tubing, similar to the transfer time T_0 of refs. 4–8, with the difference that in refs. 4–8 it had to be obtained experimentally, whereas in the present work it can be calculated with the following analytical expression:

$$\mathrm{tof} = \frac{L}{\bar{v}_p} \quad (12)$$

Obtaining the particle velocity distribution permits one to model transient signal profiles as TOF profiles. However, the signal intensities are experimentally acquired as a function of time, which is equivalent to plotting TOF distributions as a function of 1/velocity (time $\propto$ 1/velocity). Hence, one obtains the particle-dependent signal profiles after solving eqn (7). The analytical solution of the first order partial differential equation given above (eqn (7)) is available with the boundary condition for $v(t = 0) = v_0$, as follows:

$$\begin{aligned} v_p(t) &= (1 - e^{-\phi t})\left[-\frac{\nabla p}{\rho\phi} + v_f\right] + v_0 \cdot e^{-\phi t} \\ &= (1 - e^{-\phi t})\left[\frac{4C_{\mathrm{slip}}d_p^2 F}{9\pi R^4} + v_f\right] + v_0 \cdot e^{-\phi t} \end{aligned} \quad (13)$$

The second equation on the right-hand side is an explicit form, which contains only experimental parameters. The pressure drop for the laminar flow along the tube was expressed using the *Hagen–Poiseuille* equation (which relates the stationary flow of incompressible uniform viscous fluid through a channel with constant circular cross-section[16]) combined with eqn (6).

Eqn (13) describes the laser-induced aerosol transport velocity along the tubing, containing setup-related parameters (*i.e.*, tube radius R), carrier gas-dependent parameters (*i.e.*, flow rate F), and particle-relative properties (*i.e.*, particle size d_p). The first term, enclosed in parentheses, shows that the particle accelerates up to a terminal velocity value across a certain entry distance. In principle, for tubes much longer than this entry distance the velocity should increase and remain constant throughout. The second term in eqn (13), enclosed in brackets, shows the particle velocity dependency on the cross-section, slip coefficient, tube radius, and fluid flow rate. For large particles the 'no-slip-condition' (*i.e.*, gas velocity at the surface is zero) combines with a pronounced drag force due to a large cross-section. On the contrary, the drag force is low for the finer particles, but these might meet the slip condition and a modest push supports their transport. The combined effect of push and drag determines the effective motion of particles with a certain size. Finally, the last term in eqn (13), shown as an addend, is obtained with the boundary condition $v(0) = v_0$, which is the particle speed before aerosol entrainment, *e.g.*, due to ablation expulsion. The exponential decay shows that this term can be important only in the early stages of aerosol entrainment.

Returning to eqn (11), the amplitude of the signal is given only by the factor $2k$ (here to simplify $\mathscr{R}_{\mathrm{ICPMS}} = 1$), with k the flush rate as given in eqn (9). This term results from the assumption of mass conservation, *i.e.*, the area subtended by the signal profile must equal the ICP-MS integrals. Finally, the term $h(t - tof)$ is the *Heaviside function* to account for background-corrected signals, as is fully explained elsewhere.[28]

Eqn (11) is qualitatively similar to eqn (10) used in ref. 10, but quantitatively eqn (11) is more accurate in both the mathematical and physical respects. It should be remarked that the signal amplitude is accurately expressed here, which permits more detailed description of the signal profile.

Repeated shots. In normal LA-ICP-MS measurement, the experiment is performed by means of several laser pulses delivered at a constant repetition rate (*e.g.*, 10 Hz). Under this scheme, each signal data point receives the "filling contribution" of the last pulse and the "eluting contribution" of all previous pulses not yet evacuated from the setup, as explained in detail in ref. 28. The combined signal profile, resulting from a series of pulses at a given time interval, or repetition rate, is calculated from the convolution integral involving the single shot profile $I_{\mathrm{pulse}}(t)$ and the pulse delivery distribution function $S(t)$, which we recall is the following integral:

$$I(t) = \int_0^t S(\tau) \cdot I_{\mathrm{pulse}}(t - \tau)\mathrm{d}\tau \qquad (14)$$

The sample delivery function $S(t)$ can be visualized as the function that states when a certain sample pulse occurs, for how long, how high, and at what rate the whole sequence is delivered. For standard LA-ICP-MS systems, the pulse delivery distribution is a steady rate sequence of identical pulses (*i.e.*, reproducible and identical amplitude, phase, width), with a pulsation period $T = 1/f$ determined by the laser pulse repetition rate f (*e.g.*, for $f = 10$ Hz, $T = 100$ ms). It should be said that for technical reasons real pulses are known to fluctuate according to the instrument jitter, but this does not invalidate the present discussion: by knowing exactly the jitter function we can model the signal in infinitesimal detail. The sample delivery function $S(t)$ was modelled as a sequence of Gaussian pulses between the 'begin' (t_{start}) and 'stop' (t_{stop}) time, as:

$$S(t) = \sum_{n=0}^{N} \frac{1}{\tau_{\mathrm{p}}\sqrt{2\pi}} \cdot e^{-\frac{(t-n/f)^2}{2\tau_{\mathrm{p}}^2}} \qquad (15)$$

The function is Gaussian of width $\sigma = \tau_p$, which is displaced horizontally at each $(n + 1)$-th pulse, of an interval $T = 1/f$, from the previous n-th pulse. The initial pulse of the series was the $n = 0$, located with its maximum at $t = t_{\mathrm{start}}$ (*i.e.*, the beginning of the laser firing), and the last pulse of the series is the N-th, which was located at $t = t_{\mathrm{stop}}$ (*i.e.*, the end of the laser firing). The total number of pulses can be obtained from the rounded-off ratio between ablation duration and pulsation period, *i.e.*, $(t_{\mathrm{stop}} - t_{\mathrm{start}})/T$.

Table 1 Standard parameter settings used for the simulations. Different values were used only if indicated in the text

Parameter	Value	Parameter	Value
Gas type	Ar	Gas flow rate/L min^{-1}	1.0
Gas density/kg m^{-3}	1.67	Transport efficiency (%)	63.2
Gas viscosity/Pa s	2.09×10^{-5}	Cell volume/cm^3	10
Sample type	Copper	Dead volume/cm^3	0.15
Sample density/kg m^{-3}	8960	Tube diameter/mm	4.0
Particle size/nm	200	Tube length/m	1.0

Computational conditions

The parameter settings used in the simulations are summarized in Table 1. During the investigation of the effect of the individual parameters, only one parameter was scanned in a certain range, whereas the others were kept constant at the value given in Table 1. This approach might sometimes be idealistic, due to the fact that some parameters are interrelated in real experiments and changes in one imply also a modification of the other(s). However, this approach turns out to be effective for displaying the specific effect of individual parameters on signal characteristics.

Several carrier gases were simulated, whose physical properties were obtained from refs. 31 and 32 at 101 325 Pa and 288.15 K. Mean free path data were calculated from collision cross-sections, at identical pressure and temperatures. Gas data are summarized in Table 2.

Results and discussion

Carrier gas flow characteristics

Different carrier gases have been investigated experimentally in the literature and significant differences have been shown in terms of signal characteristics.[33] Unfortunately, in all experimental studies there is this intrinsic limitation, *i.e.*, the difficulty of unravelling the gas effect in the transport and in ICP-based atomization. As a first step to investigating sample introduction, we were interested in the *flow characteristics* across the transport tube. This is important because it determines several physical effects, *e.g.*, velocity profile, laminar *versus* turbulent regime, particle trajectory, *etc.*, and also the extent of computational effort for a realistic simulation.

Table 2 shows that the heavier gases require a longer time to attain full development of the flow profile. We could calculate that the carrier gas flow profile at $t = 100$ ms is, in the case of He, already fully developed, whereas Ar has a boundary layer

Table 2 Physical constants used for the various carrier gases[31,32] and times for attaining a fully developed flow profile (entry distance)

Carrier gas	Density/ kg m^{-3}	Viscosity/ μPa s^{-1}	Mean free path/nm	Development time/ms
H_2	0.085	8.6	125	39
He	0.169	18.6	193	36
N_2	1.185	16.5	66	290
O_2	1.354	19.0	72	350
Ne	0.853	29.7	140	110
Ar	1.67	20.9	70	310
Kr	3.55	23.2	54	610
Xe	5.584	21.1	46	1060

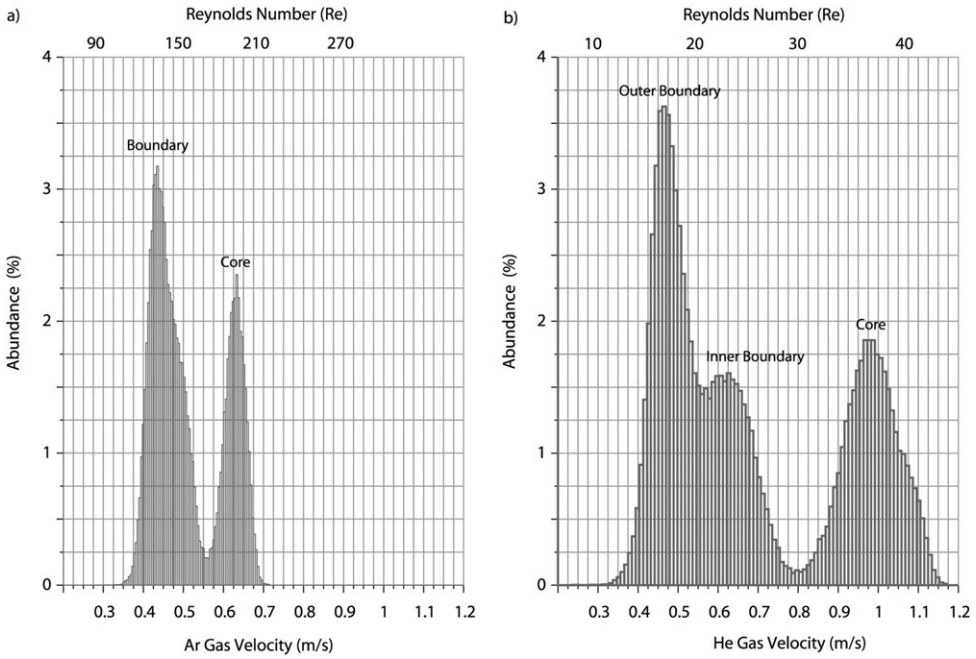

Fig. 2 Gas velocity distribution for Ar (a) and for He (b) calculated with the CFD code. The flow is split in coaxial cylindrical regions, from the boundary to the core, of increasing speed. The top axis gives corresponding Reynolds number for the specific gas and tubing used.

thickness of 1.1 mm (not shown), which is still about half the tube radius. Thus, the velocity profile as well as the boundary layer thickness is very different for the various carrier gases and, in general, the heavier gases guarantee more uniform transport conditions as a function of radial distance than the lighter gases. Hence, our results suggest that for long or wide transport tubing it is recommended to use high-mass gases (*e.g.*, Kr, Xe), which turn out to have more uniform velocity profiles over a longer transport distance. The beneficial use of He seems to be mostly justified as far as ICP atomization effects are concerned (*e.g.*, 10-fold better thermal conductivity than Ar), and should ideally be used as make-up gas.

Fig. 2 shows the gas velocity distribution for Ar (a) and He (b) in the 4 mm id tubing, with an inlet gauge pressure of 50 Pa. The full range of velocities is 0.4–0.7 m s^{-1} for Ar and 0.4–1.1 m s^{-1} for He, which is in agreement with experimental results.[8] The maximum velocity of He is a factor of 1.7 greater than that of Ar, hence He provides faster sample introduction and signal rise.

The gas flow was found to be structured in coaxial domains. In the case of Ar, there are two nested flow-cylinders. At the boundary the slower one flows with a speed of 0.35–0.55 m s^{-1} (Fig. 2(a)), which is influenced by the friction with the walls. The friction factor (φ) for laminar flow can be obtained analytically, and it is $\varphi = 64/Re$.[16] The boundary flow-cylinder has a slight positive tailing in the velocity distribution (Fig. 2(a)) because the *lowest* velocity at the wall (*i.e.*, $r/R = 1$) is a *cut-off* value. In the middle of the tube, a faster flow-cylinder moves at a speed of 0.55–0.70 m s^{-1}. This axial flow-cylinder plugs through the boundary flow-cylinder and moves faster because the peripheral friction is almost insignificant. The slight negative tailing of the velocity distribution for the core flow is because the *maximum velocity* at the tube axis (*i.e.*, $r/R = 0$) is the *cut-off* value.

The case of He (Fig. 2(b)) is more complex, because together with two broad and partially overlapping peaks at approximately 0.5 m s^{-1} and 0.6 m s^{-1}, we found a third one at speed values of 0.8–1.2 m s^{-1}. Hence, the flow structure comprises a boundary flow-cylinder and a nested inner flow-cylinder, which is split into two sub-cylinders. The central flow-cylinder moves twice as fast as the outer boundary flow-cylinder, and between the two we found an inner boundary region. Fig. 2 also shows the gas-specific Reynolds numbers (*Re*) in the specific transport tubing used (see top axis). The range of all *Re* values is well within the domain of laminar flow, which is in agreement with assumptions made so far in the literature.[4–7,12,13] However, He provides a more laminar condition in spite of the higher velocity, due to a factor of 10 lower mass density.

Fig. 3 shows the CFD numerical solutions of the gas flow profiles, together with the ideal parabolic profile that one obtains from eqn (2). The parabolic analytical solution overestimates the characteristics of the flow, due to an incomplete account of dissipative forces (*e.g.*, viscosity, wall friction, *etc.*). The numerical solutions (here the envelope is shown) visualize the complex discussion on the flow structure, showing that the radius of the core flow region is, for Ar, approximately 1 mm ($r/R = 0.5$), whereas for He it is as thin as 0.2 mm ($r/R = 0.1$). It should be noted that part of what was the "core flow-region" for Ar, in the case of He is to be considered as an *inner* boundary region. However, as a general observation, the flow speed of He is higher than that of Ar. Such a nested flow structure, *i.e.*, with an outer sheath and an inner plug flow, is in agreement with what was reported in refs. 12 and 13. In fact, the inner regions, due to the higher gas speed, guarantee better transport characteristics. Particles that might concentrate in the boundary region would not be efficiently delivered to the ICP source.

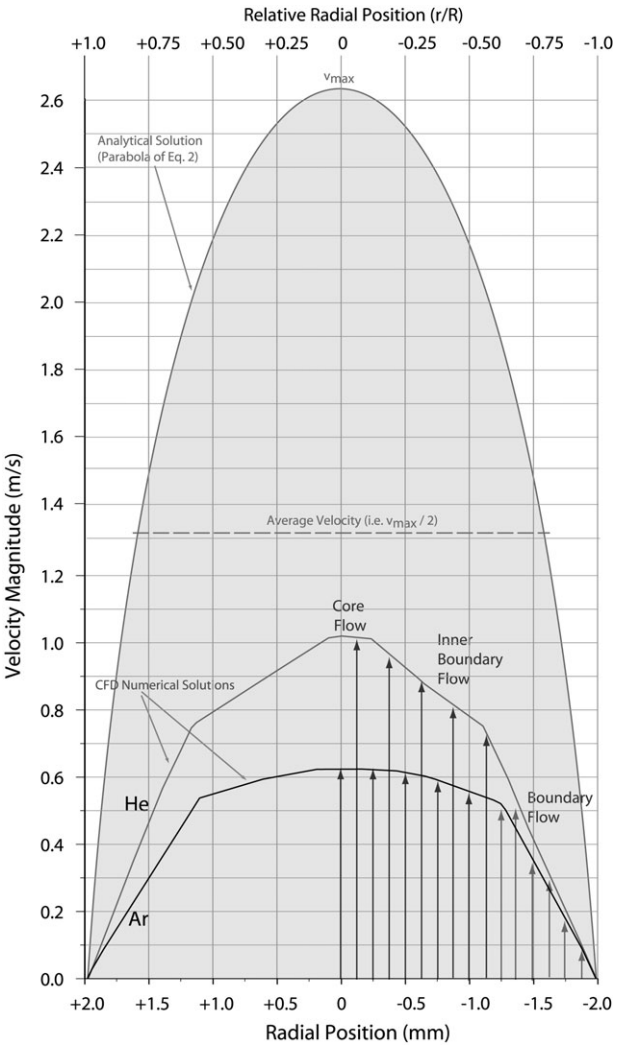

Fig. 3 Gas velocity profile for Ar and for He calculated with the CFD numerical code, and analytical parabolic solution as obtained from eqn (2). Two nested regions, *i.e.*, a slower boundary and a faster core region, characterize the flow of Ar. The flow structure for He is more complex, due to the separation of an inner boundary and a thin core flow region.

In Fig. 4 the static pressure across the tube length and the *longitudinal* velocity profiles, *i.e.*, from the tube entrance downstream up to its end, are given along three parallel directions that differ in radial position, *i.e.*, the *tube bottom* (with relative radial distance $r/R = 0.95$), along the *tube middle* ($r/R = 0.65$), and along the *tube axis* ($r/R = 0$). The tube axis shows what the local maximum velocity is. One notes that the average value is practically constant, which is determined by the constant tube radius (continuity law). The quasi-parabolic profile discussed above explains the different average value along the three plotted directions. However, one notes that high-order fluctuations are present (<1 mm), which are important in terms of the sample introduction stability. In order to improve signal characteristics, and the analytical figures of merit (*e.g.* DL), it is very important that the sample delivery is continuous and stable. Strategies to correct for this effect using an internal standard are effective and recommended, provided that reliable internal standard(s) is/are available for all analytes.

Effect of operating conditions on signal intensity

Fig. 5 shows the effect of gas flow rate (a), tube length or diameter (b), observation time (c) and particle size (d) on signal intensity. In Fig. 5(a) one notes a steady increase of signal up to 1.2 L min^{-1}, where the signal increase rate begins to slow-down. At and above 1.5 L min^{-1} the signal increase almost forms a plateau and is more and more comparable to the measurement precision. This model focuses on sample introduction and does not consider that the overall tendency at high flow rates is towards poorer sensitivities, due to pronounced ICP cooling effects.

Fig. 5(b) shows the variation of time integrated signals as a function of tube length for several tube diameters. One notes that the dependence is influenced by the signal structure, as shown in Fig. 5(c). Narrow tube widths (*e.g.*, $D = 1$ mm) produce sharp and high signals, less affected by the length of the transport tubing because for narrow tubes the total volume increase as a function of tube length is modest. Thus, uniform dispersion conditions are kept over large tube lengths. Owing to the power of four dependency of the pressure drop on the tube radius (*i.e.*, the *Hagen–Poiseuille law*[16]), a small reduction in tube width dramatically improves the transport characteristics for a given gas and flow rate. Wide tube cross-sections (*e.g.*, $D = 8$ mm) produce more prominent deterioration of sensitivity, poorer reproducibility, and worse DLs. Moreover, considering the periodic replacement of laboratory equipment, narrow (and short) tubing guarantees better comparability of results obtained at different times over long periods.

Fig. 5(c) shows simulated single-shot LA-ICP-MS intensity profiles for different sample chamber volumes in the range from 1 to 70 cm^3. Although, due to the interplay of factors, the variation of the volume also affects the transport efficiency and the dead volume, the curves were plotted for identical conditions other than volume. One notes that the small sample cell greatly reduces signal dispersion, which improves the quantitation capability. As is known, under counting statistics limited conditions the relative precision improves with the square root of signal intensity above the blank level. Thus, in experimental determinations the signal noise, which is absent in our simulations, significantly limits the implementation of large volume ablation cells where the signal intensity is slightly above background level. In fact, signal profiles obtained in large volume cells tend to be less and less distinguishable from the blank level as the cell volume increases. Because of the absence of random noise in the simulation this effect is not visualized in Fig. 5(c). Although sharp signals are characterized by improved SNR, large volume cells produce signals that tend to be more stable over time, which is important for slow scanning detection systems (*e.g.*, sector field instruments) in order to reduce spectral skew.[34]

Furthermore, the *transport efficiency* is another important parameter that accounts for the flow pattern across the ablation setup. In fact, setups of identical volume but completely different design might lead to great differences in terms of signal profiles because of different fluid-dynamical

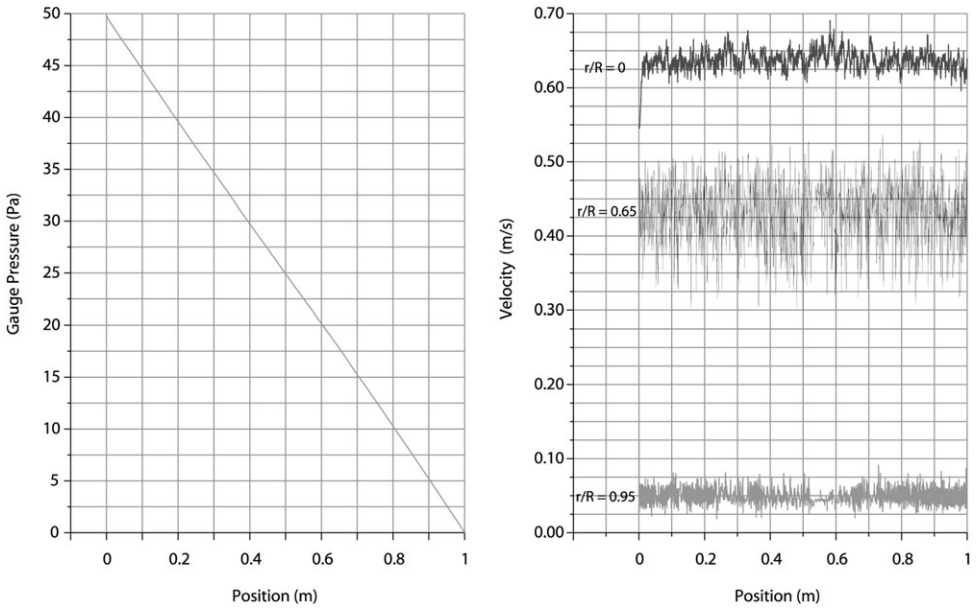

Fig. 4 Longitudinal profiles of the static pressure (left-side) and gas velocity (right-side) calculated with the CFD code, along three parallel directions. The velocity is characterized by high frequency fluctuations in the magnitude.

characteristics. Thus, for any identical flow rate and effective setup volume, two setups with different transport efficiencies will have different signal profiles.

The mass density of the ablated material influences the gravitational settling of the particles. The particle gravitational settling tends to accumulate the particles along the bottom wall of the tubing, especially the heavier particles. This might influence the mean particle drift-velocity along the transport tube, if fine and heavy particles have different radial distributions across the tubing. Fig. 5(d) shows time integrated

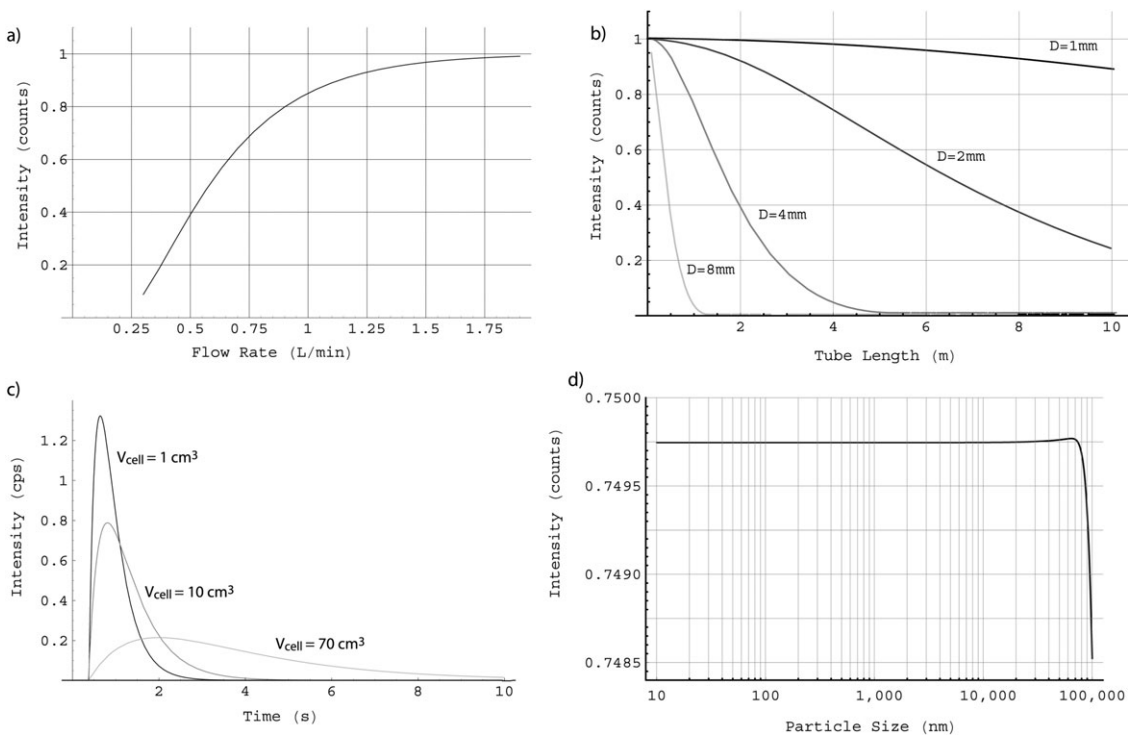

Fig. 5 Signal intensity as a function of operating conditions. (a) Calculated time-integrated signal intensity as a function of carrier gas flow rate, calculated with the own written code. This curve does not consider cooling effects in the ICP discharge, which influence the overall signal intensity. (b) Calculated time-integrated signal intensity as a function of tube length for different tube widths, calculated with the in-house written code. (c) Calculated signal intensity profiles as a function of time for single shot analysis, obtained in combination with different ablation cells volumes, as calculated with the in-house written code. (d) Time-integrated signal intensity as a function of particle size. For copper particles smaller than 70 μm no significant change of signal structure and transport time was observed. Calculation settings are given in Table 2.

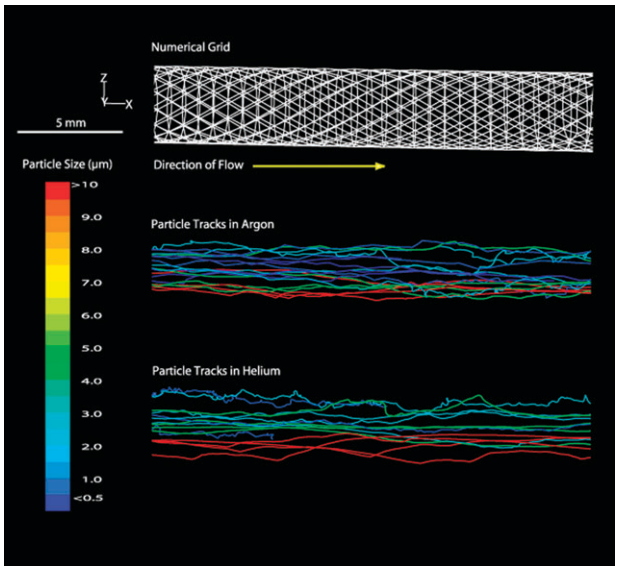

Fig. 6 Particle trajectories in the tube (the numerical grid is shown for reference) with either Ar or He as the carrier gas, calculated using the CFD code.

signal intensity as a function of particle size, *i.e.*, considering the signal profiles produced by the transport of individual particle classes. Similar or even identical signal profiles were calculated for particle sizes up to 70 µm, using copper as the target. These computational results were obtained by assuming a homogeneous distribution of all particles across the tubing, so that the velocity of drift was controlled by the gas velocity. In this way we focused our calculation on the particle size-dependence of the signal profile. However, as was said above, some parameters are interlaced, and large particles might also be slower than the fine ones, because they concentrate along the tube bottom. To verify this possibility, we modelled particle trajectories along the transport tubing in Ar and He as a function of particle size.

Particle trajectories across the tubing

Fig. 6 shows a side view of the simulated particles in tubing trajectories, with particle sizes highlighted by different colours. As a first general observation one notes that the trajectories of the finer (copper) particles are less straightforward than those of the heavier particles. This did not, however, influence the transport efficiency, which was in general close to 99% for the open tube condition. It should be said that in our model the walls of the numerical grid were reflecting barriers, so that losses due to particles sticking to the tubing were not accounted for. In the case of the SBSR-packed tubing (see below), the transport efficiency dropped significantly to 5%.

As a second statement, one notes that the heavier particles move by so-called *saltation* along the tube bottom, whereas the finer ones are suspended in the gas. However, in the case of Ar as carrier gas, the size-dependent separation is less strong than in the case of He as carrier gas. Moreover, in the case of He the fine particles follow whirling traces, and the larger particles experience long-step leaps with collision with the walls. This effect should be attributed to the higher flow velocity of He compared with Ar, and the more complex flow structure in parallel lanes.

In conclusion, one observes that Ar provides essentially size-independent transport efficiency. In the case of He, the transport of fine particles is less efficient, in a short period of time, than that of the large particles, due to the erratic trajectories. This result can be physically motivated with the longer mean free path of He *versus* Ar (Table 2), and more pronounced slipping effects for the finer particles.

Modified transport setups

Commonly, a second gas input line (the so-called *make-up gas*) is connected to the carrier gas tubing to control the flow along the tube independently from the flow in the ablation cell, or to add a feeding gas for the ICP source. Fig. 7(a) shows the pressure distribution (left-side) and gas velocity (right-side) when a make-up gas of 0.6 L min^{-1} is merged 50 cm downstream (as schematically highlighted with the shaded area). At the location of the T-junction, the static pressure was found to drop by approximately 200 Pa m^{-1}, *i.e.*, a factor of 4 higher than otherwise (Fig. 4), which caused a rapid local increase of gas velocity. However, the T-junction fitting caused a local restriction of the tube cross-section, so that the velocity at $r/R > 0.75$ is zero (the tube cross-section was 4 mm, whereas the fittings cross-section was 3 mm), and gradually increasing toward the tube axis.

Further downstream from the T-junction, the velocity rises by approximately 15–20% due to the increase of gas flow in the carrier line. This causes the sample introduction to become faster, although fluctuations from the input and make-up gas lines superpose.

In order to homogenize the velocity profile and improve transport characteristics, Moenke-Blankenburg *et al.*[4,5] suggested packing the transport tubing with spheres of up to 80% of the tube radius, using the so-called *single bead string reactor* (SBSR). In our CFD simulations, a sequence of 100 spheres was placed inside the tubing, so that a fully developed flow would interact with the SBSR. The individual spheres were exactly 60% of the inner tube diameter, *i.e.*, 2.4 mm, and displaced so that they were lying upon the tube bottom. Fig. 7(b) shows the results obtained, where the shaded area indicates the SBSR location within the one-metre tubing. The static pressure shows (left-side), after a modest linear decrease at the entry (*i.e.*, 32 Pa m^{-1}), a more dramatic linear drop of 100 Pa m^{-1} all over the SBSR region. The velocity was, as expected, more uniform from the axis ($r/R = 0$) to the border ($r/R = 0.9$) than in the open tube condition (Fig. 4). In the latter case, the gas velocity at the axis might vary by a factor of 10–15 from that at the border. In the case of the SBSR-packed tube, we found a difference of a factor of 5 between axis and border gas speed (Fig. 7(b)). It should also be noted that the fluctuations had much higher amplitude than in the case of the open tube. Further calculations, made by modifying the radius of the spheres, resulted in a similar conclusion as is made here.

Moreover, the transport was hindered along the axis due to the barrier created by the beads. Thus, the particle trajectories were forced towards low-speed areas, *i.e.*, the boundary, as long as a sudden trajectory change was possible. In fact, the

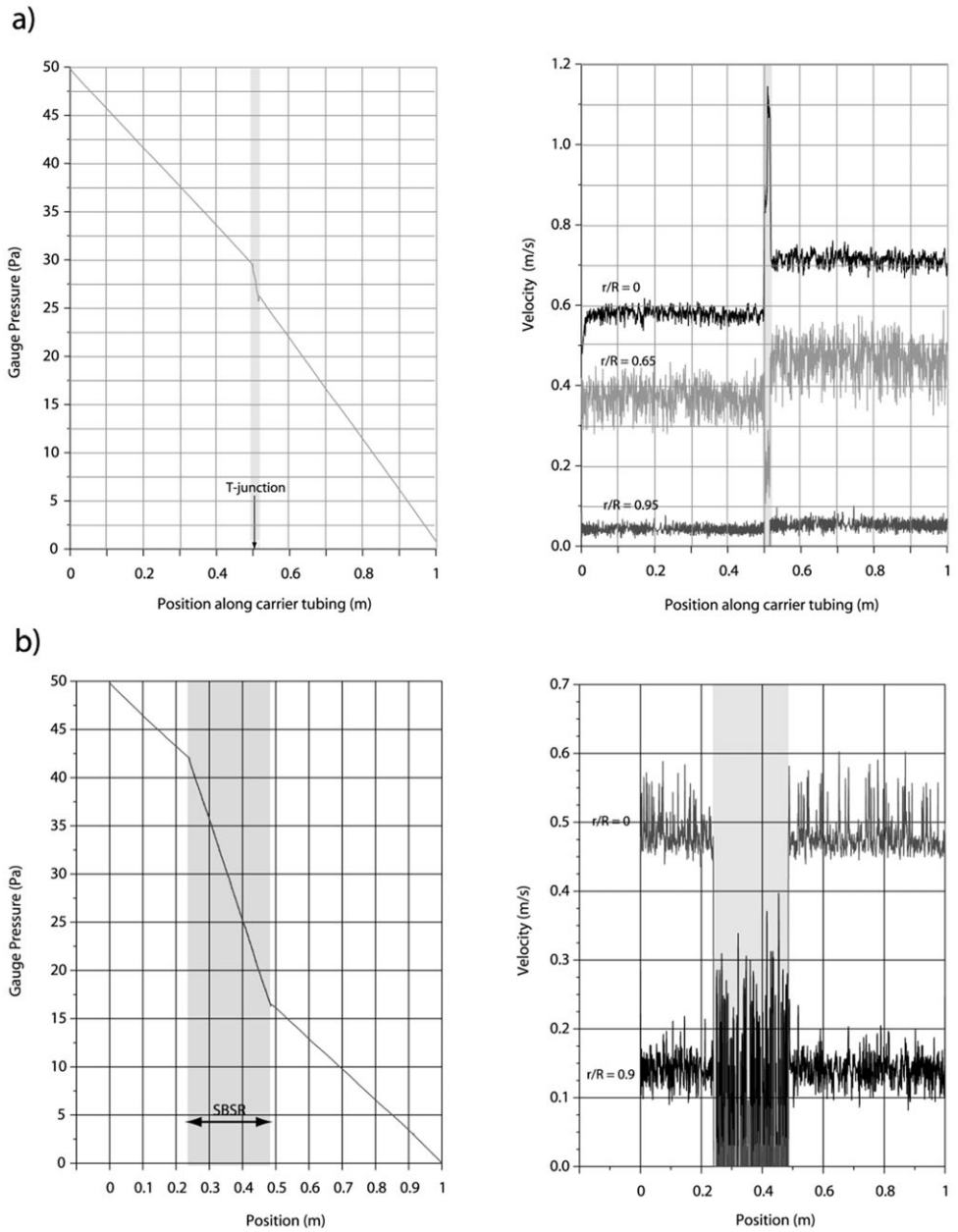

Fig. 7 (a) Longitudinal pressure (left-side) and gas velocity profile (right-side) calculated with the CFD code, for a T-junction 50 cm downstream (shaded area) with a make-up gas at 0.6 L min^{-1}. (b) Longitudinal pressure (left-side) and gas velocity profile (right-side) calculated with the CFD code and using a SBSR (shaded area).

simulations revealed that the beads were just a *deflecting* obstacle for the *fine* particles, whereas for the *larger* particles the beads were a *stopping* obstacle. For the coarse particles the transport efficiency dropped dramatically as a function of the number of beads, and with our 100-beads simulation it was reduced to almost zero.

Transient signals from multiple pulses

Convolving the signals for the single shot intensity profile with the pulse delivery distribution, as explained in the computational model section, we could obtain the transient intensity signals from multiple pulses, *i.e.*, the sample introduction *versus* time. Signals simulated for 1 Hz (a), 5 Hz (b) or 10 Hz (c) pulse repetition rate with a pulse width 50 ms (*i.e.*, the above-mentioned *pristine time-spread*) are shown in Fig. 8, together with the actual pulse delivery. The signal produced at 1 Hz (a) repetition rate has a periodic profile, since the tips of the single shots are narrower than the pulsation period, and hence can be resolved.

On the other hand, a pulse repetition rate of 5 Hz (b), or even more 10 Hz (c), produced more strongly overlapping pulses (pulse incubation) and stable signal profiles. The average signal intensity increases linearly from 1 to 10 Hz because

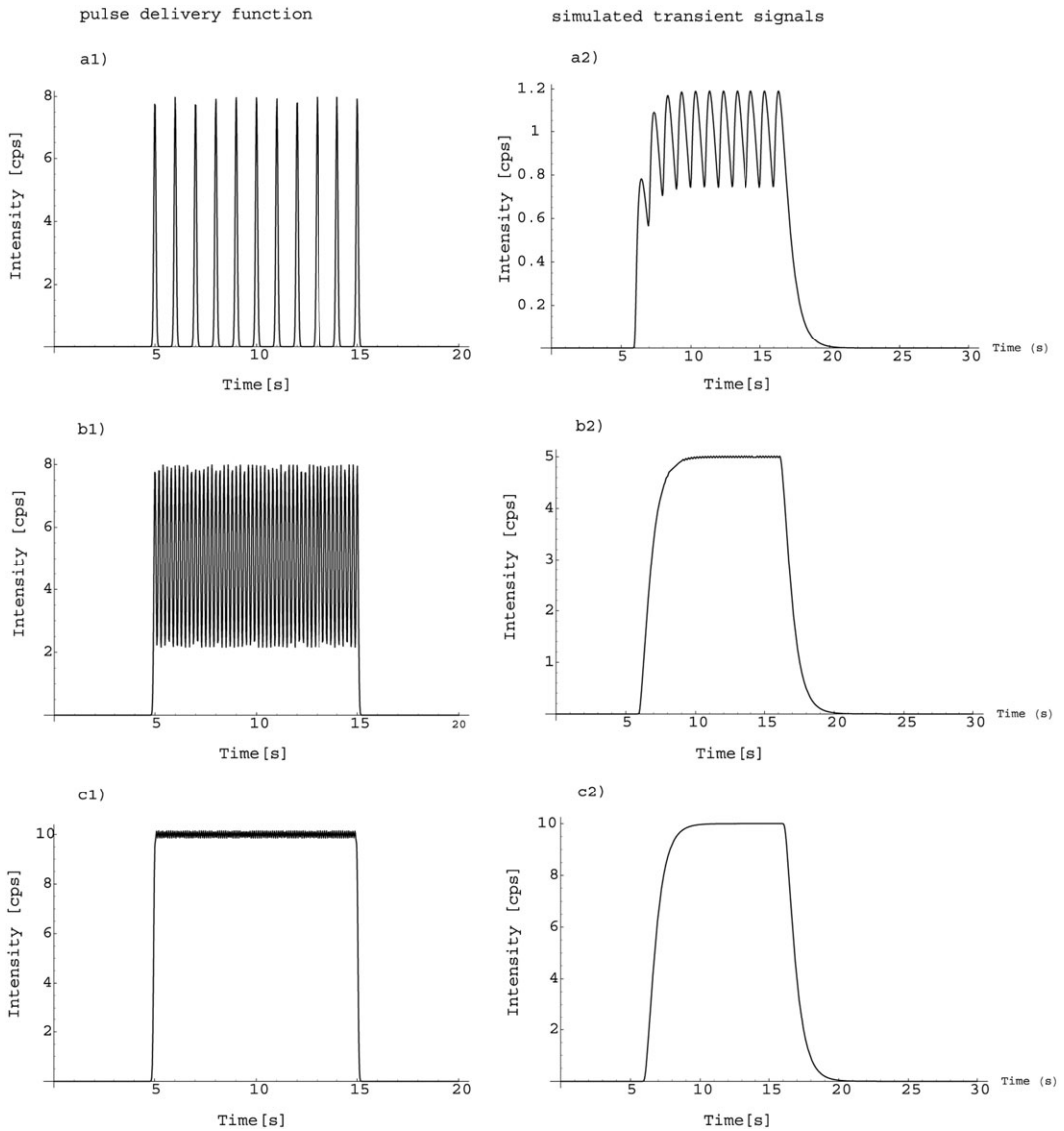

Fig. 8 Pulse sequence at 1 Hz (a), 5 Hz (b), 10 Hz (c) pulse delivery (left-side) and the transient signals obtained (right-side), calculated with the in-house written code.

by higher repetition rate also the *duty cycle* increases. It should be recalled that the duty cycle is the ratio between the pulse duration and the unit measurement duration, *i.e.*, $\tau_p / [(t_{stop} - t_{start})/n] = \tau_p/T = \tau_p f$. Hence, if the single shot is normalized and the duty cycle is 50%, then the transient signal has an average intensity of $I = 0.5$.

Conclusions

Computer simulations using a fluid-dynamical numerical code were created to investigate the transport of laser-induced particles during sample introduction for ICP-MS analysis. The flow regime was found to be laminar, with a mean velocity of few tens of cm s^{-1} at standard operating conditions. The flow develops into a nested parabolic profile in a few tens of cm. This effect was shown to be strongly a function of carrier gas molecular weight. However, the velocity was found to be fluctuating along the tube length, which causes deterioration in the time-dependent sample introduction. The use of an internal standard is therefore always recommended.

An in-house-written original code was used to simulate the interplay of operating parameters that contributes to the observed LA-ICP-MS signal profile. A major influence on signal characteristics is to be attributed to the setup characteristics, namely, dimension and shape of cell and transport length. The minimum time width of single shot signals can be calculated by dividing the transport distance by the carrier gas terminal velocity (particle TOF). For the present case, a carrier gas moving at 0.6 m s^{-1} across one metre long tubing will produce a signal whose width cannot be shorter than 1.6 s. This is so because the time width of the intensity signal is the spread of particle arrival at the detector. Considering diffusion-dominated dispersion, *i.e.*, the particles fill the free volume homogeneously, the minimum time spread is calculated from the transport of the first and last particle along the tube. Hence, the fluid-dynamical characteristics of the setup, *i.e.*,

how efficiently the carrier gas sweeps the geometrical volume, are also very important. Small setups of poor design, *e.g.*, presence of angularities, small outlet orifices, *etc.*, might perform similarly to large setups of improved aerodynamics. Furthermore, the use of junctions, or barriers, along the streamlines (*e.g.*, SBSR) perturbs and often deteriorates the transport efficiency. The transport efficiency was shown to appear as an argument of a logarithmic function in the relation between signal intensity and parameter settings. Hence, its importance needs to be stressed in the description of transient signals, especially for setups of small dimension, or even for in-torch ablation.

Finally, the transient signals obtained by means of repeated delivery of laser pulses at constant repetition rate was shown to be the result of convolution of the single shot signal profile with the pulse delivery progression. At high repetition rate, *i.e.*, when the pulse delivery period is shorter than the single shot width, we found a condition of pulse incubation that homogenizes the profile.

Acknowledgements

Mrs Ch. Surber and Mr J. Glas of the EMPA-EAWAG Library are acknowledged for assistance with literature searches. Discussions with Dr A. Plotnikov (Hahn-Meitner-Institut in Berlin) and M. Tanner (ETH Zurich) have been stimulating to initiate this work. Financing from the Flemish Fund for Research (FWO) is acknowledged for the postdoctoral fellowship of D. Bleiner.

References

1 D. Günther and B. Hattendorf, *Trends Anal. Chem.*, 2005, **24**, 255–265.
2 K. Meissner, Th. Lippert, A. Wokaun and D. Günther, *Thin Solid Films*, 2004, **453–454**, 316–322.
3 J. S. Becker, *Spectrochim. Acta, Part B*, 2002, **57**, 1805–1820.
4 L. Moenke-Blankenburg, *Spectrochim. Acta Rev.*, 1992, **15**, 1–
37.
5 L. Moenke-Blankenburg, M. Gäckle, D. Günther and J. Kammel, *Plasma Source Mass Spectrom.*, 1990, **85**, 1–17.
6 M. Gäckle and D. Günther, *Z. Chem.*, 1988, **28**, 258–260.
7 M. Gäckle and D. Günther, Dissertation, University of Halle-Wittemberg, 1990.
8 D. Bleiner and D. Günther, *J. Anal. At. Spectrom.*, 2001, **16**, 449–456.
9 D. Bleiner, PhD Dissertation nr 14665, ETH Zurich, 2002.
10 A. Plotnikov, C. Vogt and K. Wetzig, *J. Anal. At. Spectrom.*, 2002, **17**, 1–8.
11 A. M. Leach and G. M. Hieftje, *Appl. Spectrosc.*, 2002, **56**, 62–69.
12 M. Gäckle and D. Merten, *Spectrochim. Acta, Part B*, 2004, **59**, 1893–1905.
13 M. Gäckle and D. Merten, *Spectrochim. Acta, Part B*, 2005, **60**, 1517–1530.
14 G. Schwedt, *Analytische Chemie*, G. Thieme Verlag, Weinheim, 1995.
15 M. Guillong, I. Horn and D. Günther, *J. Anal. At. Spectrom.*, 2003, **18**, 1224–1230.
16 R. B. Bird, W. E. Stewart and E. W. Lightfoot, *Transport Phenomena*, Wiley, Chichester, 2nd edn, 2001.
17 D. J. Acheson, *Elementary Fluid Dynamics*, Clarendon Press, Oxford, 1990.
18 P. Baron and K. Willeke, *Aerosol Measurement: Principles, Techniques and Applications*, Wiley-Interscience, Chichester, 2nd edn, 2001.
19 S. G. Jennings, *J. Aerosol Sci.*, 1988, **19**, 159–166.
20 R. L. Buckley and S. K. Loyalka, *J. Aerosol Sci.*, 1989, **20**, 347–349.
21 M. D. Allen and O. G. Raabe, *J. Aerosol Sci.*, 1982, **13**, 537–547.
22 M. D. Allen and O. G. Raabe, *J. Aerosol Sci.*, 1985, **16**, 57–67.
23 S. I. Rubinov and J. B. Keller, *J. Fluid Mech.*, 1961, **11**, 447.
24 P. G. Saffman, *J. Fluid Mech.*, 1965, **22**, 385–400.
25 A. Li and G. Ahmadi, *Aerosol Sci. Technol.*, 1992, **16**, 209–226.
26 H. Niu and R. S. Houk, *Spectrochim. Acta, Part B*, 1996, **51**, 779–815.
27 G. C. Y. Chan, W. T. Chan, X. Mao and R. E. Russo, *Spectrochim. Acta, Part B*, 2001, **55**, 221–235.
28 D. Bleiner, F. Belloni, D. Doria, A. Lorusso and V. Nassisi, *J. Anal. At. Spectrom.*, 2005, **20**, 1337–1343.
29 M. Tanner and D. Günther, *J. Anal. At. Spectrom.*, 2005, **20**, 987–989.
30 X. R. Liu and G. Horlick, *Spectrochim. Acta, Part B*, 1995, **50**, 537–548.
31 D. R. Lide, *CRC Handbook of Chemistry and Physics*, CRC, Boca Raton, 83rd edn., 2002.
32 *The Gas Encyclopedia (by Air Liquide)*, Elsevier, Amsterdam, ISBN: 0-444-41492-4, 1976, 3rd reprint, 2002.
33 X. L. Mao, O. V. Borisov and R. E. Russo, *Spectrochim. Acta, Part B*, 1998, **53**, 731–739.
34 G. M. Hieftje, J. H. Barnes IV, O. Groen, A. M. Leach, D. McClenathan, S. J. Ray, D. Solyom, W. C. Wetzel, M. Bonner Denton and D. Koppenaal, *Pure Appl. Chem.*, 2001, **73**, 1579–1588.

